Journal of MATERIALS RESEARCH

Invited Paper
DOI:10.1557/s43578-022-00708-w

BORON NITRIDE NANOTUBES

FOCUS ISSUE

Tribological and neutron radiation properties of boron nitride nanotubes reinforced titanium composites under lunar environment

Nicole Bacca[1,2], Cheng Zhang[1], Tanaji Paul[1], Abhijith Kunneparambil Sukumaran[1], Denny John[1], Sara Rengifo[3], Cheol Park[4], Sang-Hyon Chu[5], Matthew Mazurkivich[3], William Scott[6], Arvind Agarwal[1,a]

[1] Plasma Forming Laboratory, Department of Mechanical and Materials Engineering, Florida International University, 10555 West Flagler Street, Miami, FL 33174, USA
[2] Department of Mechanical Engineering, Boston University, 110 Cummington Mall, Boston, MA 02215, USA
[3] Materials Test, Chemistry and Contamination Control Branch, NASA MSFC, Huntsville, AL 35808, USA
[4] Advanced Materials and Processing Branch, NASA Langley Research Center, Hampton, VA 23681, USA
[5] National Institute of Aerospace, 100 Exploration Way, Hampton, VA 23666, USA
[6] ERC Inc., Jacobs Space Exploration Group, Huntsville, AL 35806, USA
[a] Address all correspondence to this author. e-mail: agarwala@fiu.edu

Received: 13 April 2022; accepted: 15 August 2022; published online: 6 September 2022

The present study reports the tribological behavior, and radiation shielding performance of a multifunctional boron nitride nanotube (BNNT) reinforced titanium metal matrix composite (MMC) for applications in lunar exploration. BNNT-Ti MMCs showed 10.2 and 25.5% improvements in wear volume loss compared to pristine Ti samples with and without lunar simulant, respectively. For neutron radiation shielding evaluation, an additional set of samples with similar compositions was sintered at 750 °C. The decreased sintering temperature from 950 to 750 °C prevented BNNTs from interfacial reactions with the Ti matrix during sintering. The highest neutron attenuation was observed in BNNT-Ti MMC sintered at 750 °C, followed by the one sintered at 950 °C and pristine Ti sample. Maximum 45 and 50% improvements in linear and mass absorption coefficient were shown, respectively. This study proves that adding BNNTs to the Ti alloy matrix greatly enhanced the wear resistance, yield strength, and radiation shielding performance.

Introduction

Titanium and its alloys have attracted tremendous attention for their superior specific strengths, high thermal stability, and corrosion resistance [1, 2]. There are two main phases in Ti, α, and β. α-Ti has an hcp crystal structure, stable up to 882 °C. At elevated temperatures, it can transform into the β phase with a bcc crystal structure [1]. Multiple alloying routes have been developed for titanium to tailor its properties. Different alloying elements serve as α and β stabilizers. Ti6Al4V (Ti64) is the most widely used Ti alloy with high strength from the α phase and decent formability from the β phase. However, the production of titanium is challenging compared to traditional metals, such as iron and steel, due to its high reactivity [3].

Titanium is one of the most important metals for space exploration missions [4]. Unfortunately, pristine titanium or titanium alloys cannot fulfill all the needs under the extraterrestrial environment, such as the lunar surface. The environmental conditions at the lunar surface are extreme for most materials [5]. Materials are subjected to extreme vacuum, prolonged thermal cycles, harmful radiation exposures, and abrasive lunar regolith on the lunar surface [6, 7]. During the lunar landing phases, descent, and ascent, regolith particles traveling at high speeds can cause severe damage to the surface of aerospace equipment. The regolith particles vary in size and shape, depending on the lunar sites. However, they all are highly abrasive due to the lack of erosion by water and wind. Radiation shielding is another important criterion for screening materials on lunar surfaces [8, 9]. The lack of an atmosphere and magnetic field on the lunar surface means that the Moon has little shielding, allowing for harmful space radiation, such as galactic

cosmic rays (GCR), solar particle events (SPE), and secondary albedo radiation, to pass through and harm astronauts and electronic equipment. Energetic GCR and SPE particles interact with the planetary surface soil, producing a cascade of secondary particles such as neutrons [10–12]. The presence of secondary neutrons can be a potential threat to the safety of the crews and the success of space missions because the high linear energy transfer of neutrons imposes significant damage to biological cells and microelectronics at their paths [13].

Based on this scenario, we propose a multifunctional boron nitride nanotube-reinforced titanium metal matrix composite (BNNT-Ti MMCs) to address these challenges for sustainable and safe space exploration. Titanium's mechanical properties, wear resistance, and radiation shielding properties are expected to be improved by incorporating BNNTs.

Boron nitride nanotubes (BNNTs) are one-dimensional nanomaterials with a similar structure and mechanical properties as carbon nanotubes (CNTs) [14, 15]. Unlike CNTs, BNNTs possess high thermal and chemical stabilities, which allow them to be incorporated into metal matrix composites as reinforcement. Only a few studies have reported BNNTs reinforced metal matrix composites with improved mechanical performance than pristine metal and alloys. Nautiyal et al. incorporated BNNTs into an aluminum matrix and found a 400% increase in tensile strength compared to pure Al [16]. Bhuiyan et al. synthesized BNNT-Ti MMCs using pressureless sintering at various conditions. BNNT-Ti samples showed increased compressive strength under conditions of room temperature and high temperature (500 °C) [17]. Bustillos et al. introduced BNNTs into Ti64 alloy and fabricated BNNT-Ti MMCs using spark plasma sintering at various sintering conditions [18]. The relationships between the sintering conditions, the survival of BNNTs, and the interfacial reactions between BNNTs and the Ti matrix were studied. A 50% increase in compressive strength was observed in our previous work on BNNT-Ti composites [18].

For space exploration applications, the tribological behavior is another important aspect as the environment leads to a high risk for erosion due to the lunar regolith. In the limited literature on BNNT-reinforced Ti MMCs [17–19], there is no report on the tribological behavior of BNNT-Ti MMCs in ambient and under simulated lunar environments. BNNTs also have outstanding neutron radiation shielding properties because of B elements [20–22]. As pioneers in BNNT-related research, scientists at NASA Langley Research Center have proven the effectiveness of BNNTs as radiation shielding additives [23–25]. They also identified BNNTs as an important additive for future human space exploration missions. Multiple studies have reported enhanced radiation shielding properties in BNNT-contained composites, yet not a single work has been done on BNNT-Ti MMCs [23–25]. Based on this scenario, the present study investigates tribological behavior and radiation shielding properties of BNNT-Ti MMCs. The potential of applying BNNT-Ti MMCs for space exploration missions is evaluated.

Results and discussion

Microstructural analysis of pristine Ti and BNNT-Ti samples

A summary of microstructural information on BNNT-Ti composites is presented in Fig. 2. The details of the BNNT-Ti composite's sintering conditions and their effect on microstructural evolution can be found in our previous work [18].

From Fig. 1, it is concluded that the addition of BNNTs significantly inhibited the grain growth during sintering. Figure 1(b) displays the resultant grains exhibiting an elongated shape, so the grain dimension in both longitude and transverse directions is provided to understand the grain morphologies better. Nearly 50% reduction in grain size in both directions is measured in the BNNT-Ti sample. BNNT agglomeration was also observed in the BNNT-Ti sample. Figure 2 shows the polished cross-sectional SEM images of BNNT-Ti composites. The agglomeration of BNNT led to the increase in porosity in BNNT-Ti. In the BNNT agglomeration region, the grains became more equiaxed than the grains shown in Fig. 1, and grain coarsening was observed due to the poor dispersion of BNNTs in these regions. It must be pointed out that the agglomeration of BNNTs is localized and does not reflect the overall grain size information. These coarsened grains were not considered for the overall grain size measurement. Localized interfacial reactions between Ti and BNNT due to agglomeration, their thermodynamics, and TEM images are discussed in our previous work [18].

Tribological behavior of Ti and BNNT-Ti MMCs

Pin-on-disk wear

The wear test results on pure Ti and BNNT-Ti composites are summarized in Table 1. The BNNT-Ti composite displayed improved wear resistance compared to the pure Ti sample. The addition of 1 wt% BNNT reduced the coefficient of friction (COF) from 0.412 to 0.368 and mitigated the wear volume loss by 10.2%. Tribology is a surface science, and a material's wear performance is closely related to its surface hardness and yield strength. The microhardness results for both Ti and BNNT-Ti can also be found in Table 1. A bimodal microhardness was found in BNNT-Ti samples. The higher hardness observed represents most of the BNNT-Ti sample. The location where lower hardness was measured coincided with the agglomeration BNNTs, accounting for less than 10% of the entire sample area. Hence, when analyzing the wear behaviors of the BNNT-Ti sample, a single value of 4.67 GPa was taken after statistical

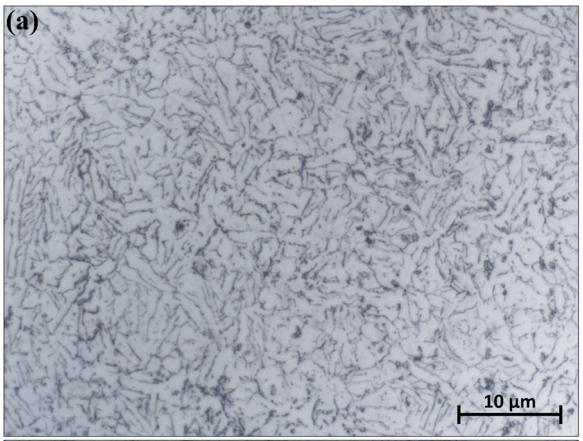

(C) Microstructural summary of pristine Ti and BNNT-Ti composites

Sample	Densification (%)	Grain Size (µm)	Microhardness (GPa)
Pristine Ti	98.7	Long: 7.4 ± 2.6 Trans: 2.3 ± 0.9	3.10 ± 0.01
BNNT-Ti	97.5	Long: 3.6 ± 1.6 Trans: 1.2 ± 0.4	4.80 ± 0.50 3.50 ± 0.20 (BN agglomerated region)

Figure 1: Optical microscope images of (a) pristine Ti and (b) BNNT-Ti after sintering at 950 °C. (c) The densification (%), grain size (µm) and microhardness (GPa) observed from the microstructure of pristine Ti and BNNT-Ti.

considerations. The increased hardness can be attributed to the reduction in grain size with the addition of BNNTs. At the current sintering conditions, Bustillos et al. found that TiB is the main interfacial reaction product instead of TiB_2 [18]. Both TiB and BNNTs can be found at the grain boundaries and pin the dislocation to increase the overall microhardness.

The SEM images of wear tracks on both Ti and BNNT-Ti samples provide insights into the wear mechanism. Figure 3(a to c) shows the wear surface of the pristine Ti sample. The overall wear scar for Ti shows deep grooves indicating plowing was the primary wear mechanism. Severe plastic deformation was observed in the wear track due to high contact pressure from the aluminum oxide ball. As the wear test progressed, the high contact pressure led to materials failure and detachment from the wear surface. Some large wear debris, up to 50 µm, was found in the wear track in Fig. 3(b). The wear debris did not roll along the surface to trigger three-body wear. Instead, the wear debris was flattened and caused localized adhesive wear. Scuffing can be seen on the wear surface as an indication of adhesive wear, as shown in Fig. 3(c). Ductility in the pristine Ti is responsible for severe plastic deformation during wear testing. The wear debris formed during wear did not pose secondary damage to the materials.

The worn surface of the BNNT-Ti composite is shown in Fig. 3(d to f). The wear surface is smoother than the one in the pristine Ti sample. Reduced plastic deformation was visible on the wear surface. The overall densification reduced from 98.7 to 97.5% when incorporating 1 wt% BNNTs. The microstructural analysis found that the BNNTs were wrapped around the Ti particles and were located at the grain boundaries after sintering. The addition of BNNTs significantly inhibited the grain growth during sintering and primarily retained the initial particle morphologies after sintering. Figure 3(e) depicts exposed wear subsurface with granular particles as a result. Despite this, these granular particles were not "loose." There is no sign of abrasive damage from the three-body wear induced by these granular particles. Microstructural analysis in our previous study indicated that BNNTs formed solid interfacial bonding with Ti particles through diffusion and chemical reactions [18]. Figure 3(f) shows flattened BNNT structures anchored across multiple grains and enhanced overall integrity. Hexagonal boron nitride is known for its outstanding lubricating property. Like the wear behavior of CNT reinforced composites, lubricating graphene sheets formed from the peeling of CNTs, the peeling of BNNTs can potentially form hBN to alleviate the lateral resistance during wear and reduce the COF [26]. However, Fig. 3(f) suggests the BNNTs were flattened and anchored on the Ti grains instead of peeling, which explains no significant reduction in COF and a high diminution in wear volume loss in the BNNT-Ti wear.

Wear with lunar regolith simulants

The results of wear testing with zircon lunar regolith simulant can also be found in Table 2. During the tests, zircon simulant particles acted as interfacial elements between the aluminum oxide ball and the composite samples and isolated the ball from the sample surfaces. Generally, the wear behavior would be alleviated in such conditions. Zircon simulant particles are the most abrasive among the lunar regolith simulants. Hence, wear tests with zircon simulant on the pristine Ti sample produced 5.16 times the wear volume than the tests without it. Similar results were yielded in the BNNT-Ti tests, where those including the zircon simulant produced 4.27 times the wear than those without it. The zircon simulant particles also caused an increase in the frictional resistance as the coefficient of friction for Ti and

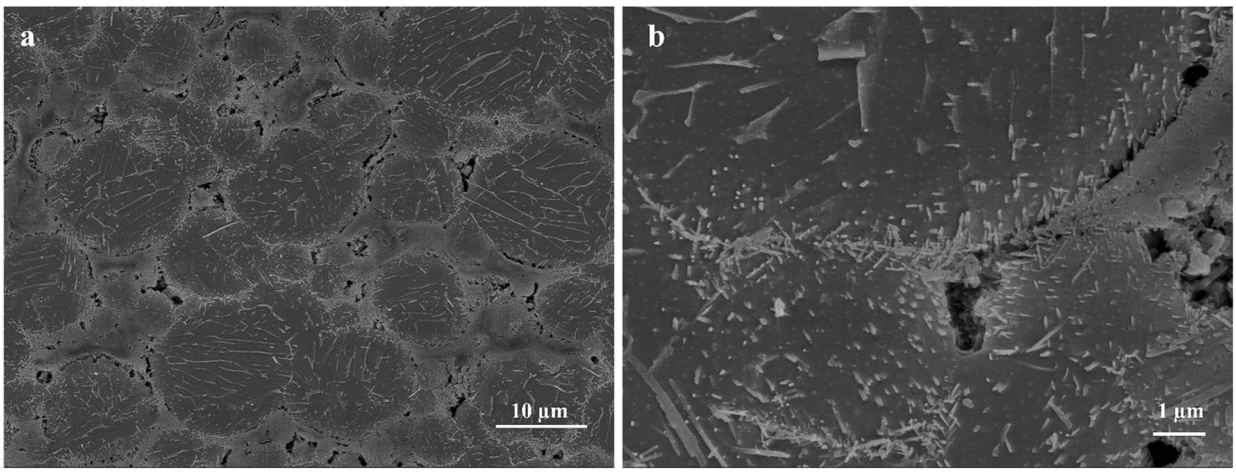

Figure 2: SEM of polished cross-sectional images of BNNT-Ti (a) and (b) high magnification.

TABLE 1: Results of tribological testing on pristine Ti and BNNT-Ti samples.

Sample	Lunar regolith simulant	Coefficient of friction	Improvement in CoF from pristine Ti	Wear volume (mm^3)	Improvement in wear from pristine Ti
Pristine Ti	None	0.412	N. A	0.049	N. A
BNNT-Ti	None	0.368	9.76%	0.044	10.2%
Pristine Ti	Zircon	0.448	N. A	0.253	N. A
BNNT-Ti	Zircon	0.434	3.13%	0.188	25.5%

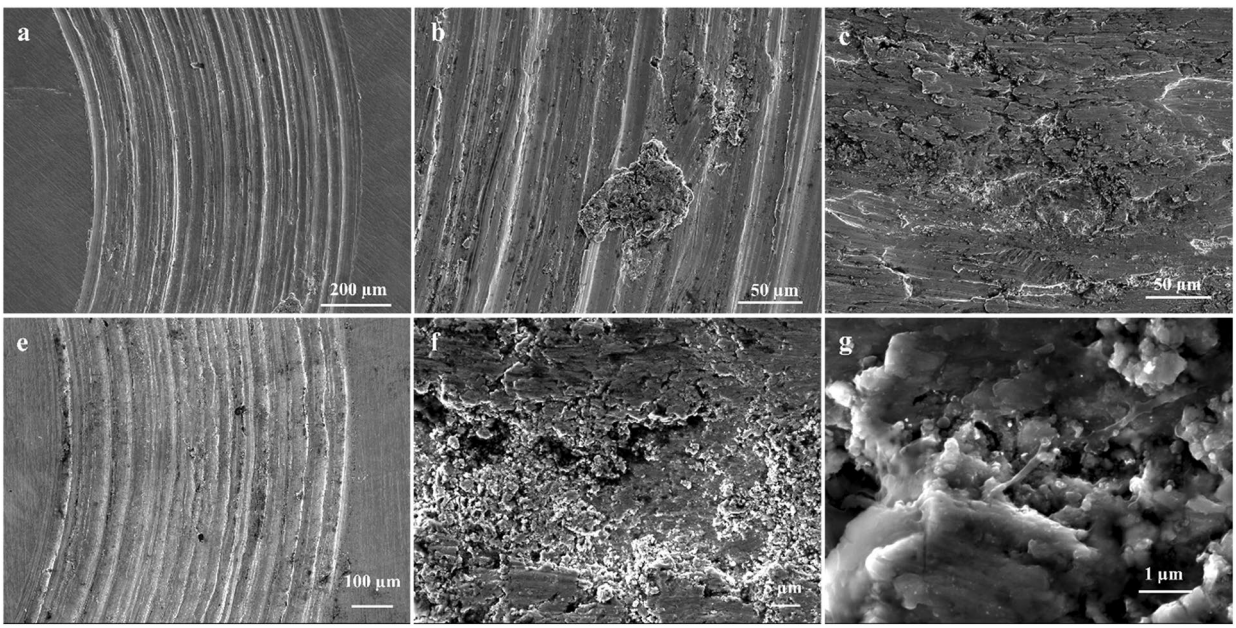

Figure 3: SEM images of wear track on pristine Ti sample: (a) low magnification image showing plowing, (b) flattened wear debris, and (c) localized scuffing. SEM images of wear track on BNNT-Ti sample: (d) low magnification image, (e) exposed granular particles, and (f) BNNT anchored on granular particles.

TABLE 2: Geometric characterization of pristine Ti and BNNT-Ti with different sintering temperatures.

Sample name	Thickness (mm)	Density (g/cm^3)	Linear adsorption coeff μ_x (mm^{-1})	Mass adsorption coeff μ_m (cm^2/g)
Pristine Ti (750 °C)	4.03	4.37 (97.1%)	0.0424	0.097
BNNT-Ti (750 °C)	3.46	4.23 (95.5%)	0.0615	0.145
Pristine Ti (950 °C)	3.60	4.45 (98.8%)	0.0431	0.097
BNNT-Ti (950 °C)	4.18	4.36 (98.4%)	0.0464	0.106

BNNT-Ti increased by 8.73 and 17.9%, respectively. Nevertheless, adding the BNNT successfully improved the wear resistance of the MMCs in the wear experiments with lunar regolith simulants. Compared to the pristine Ti sample, a 25.5% reduction in wear volume was achieved in the BNNT-Ti sample. The reduction in wear volume loss was the direct outcome of increased hardness in the BNNT-Ti sample and the anchoring effect from BNNTs, as shown in Fig. 3(f). The COF of BNNT-Ti did not show as pronounced improvement as the one in wear volume reduction; only a 3.13% difference was obtained between pristine Ti and BNNT-Ti samples.

SEM images (Fig. 4) of the wear tracks with simulants revealed the wear track to be almost double the width of those without stimulants. In Fig. 4(a and b), both wear tracks are more chaotic than the wear tests without stimulants in Fig. 3. Notably, the accumulation and embedding of zircon simulant particles are mainly on the edges of the wear scars in both samples, indicating the particles were dragged along the sides. The embedded zircon simulant particles in the Ti sample were more pointy and edgy than those in the BNNT-Ti sample, which were relatively "flat." A higher degree of crushing and fragmentation of zircon simulant particles in the BNNT-Ti sample was expected

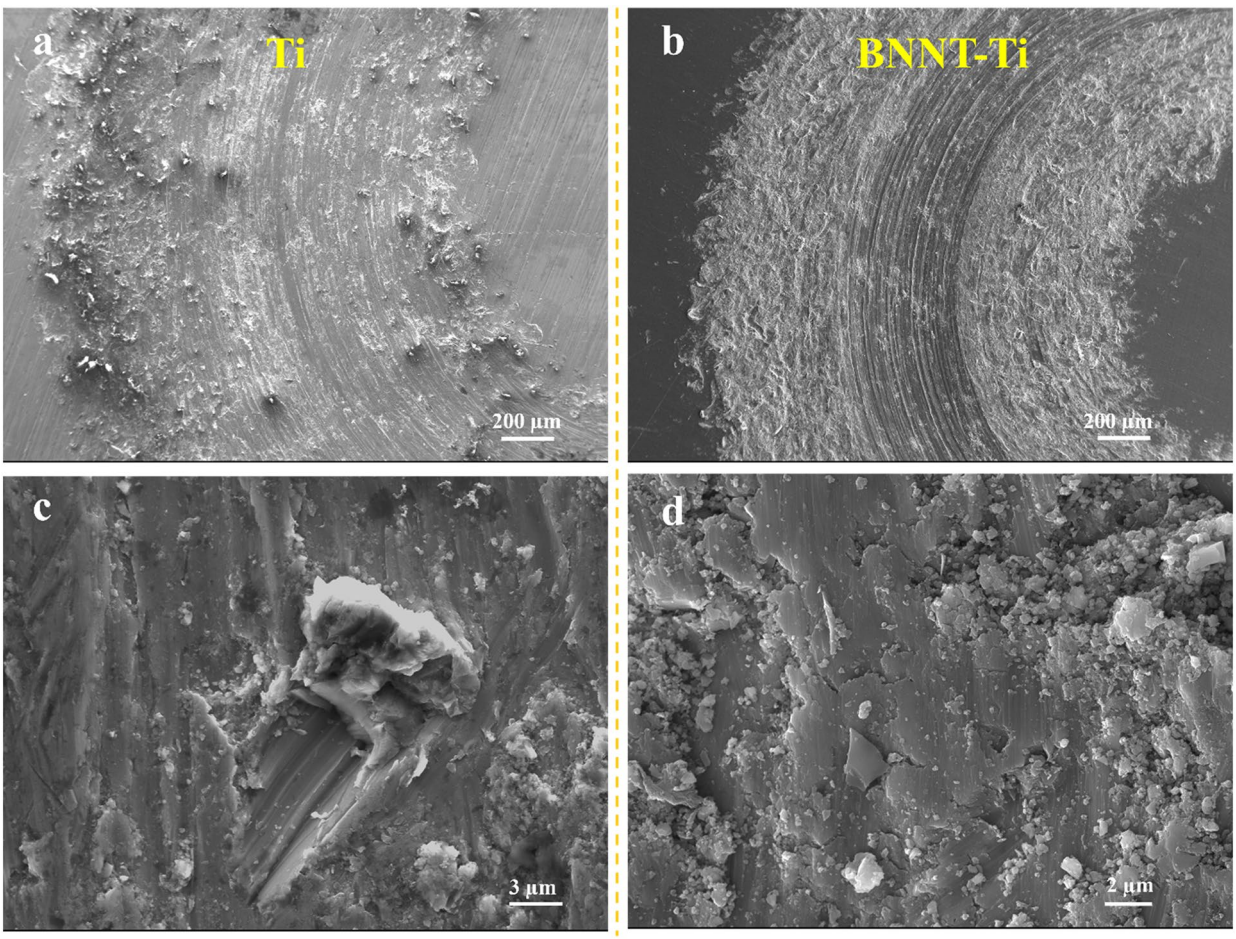

Figure 4: SEM images of wear tracks in lunar simulant presence. Overall wear tracks for (a) Ti and (b) BNNT-Ti composites. (c) Plowing is observed in pristine Ti. (d) A smoother wear surface is observed in BNNT-Ti.

due to the increased hardness with BNNTs additions. BNNT-Ti showed a smoother worn surface compared to pristine Ti. The difference became more significant in the higher magnification shown in Fig. 4(c and d). This is due to the increased hardness in the BNNT-Ti sample, which required higher energy for the embedment to occur. Both samples identified signs of plowing, suggesting that the zircon simulant particles did not roll but slid between the aluminum oxide ball and metal surfaces. The additional plowing observed in both samples, especially in the BNNT-Ti sample, increased the lateral resistance during the wear test. Hence, the coefficient of friction for both samples increased compared to the wear tests without regolith. No signs of tribo-film or any other lubricating mechanisms were detected from BNNTs. The increased hardness, strength, and anchoring effect are the main contributions of BNNTs. Thus, BNNT-Ti exhibited better wear resistances with and without lunar regolith simulant.

Yield strength of Ti and BNNT-Ti MMCs using profilometry-based indentation plastometry (PIP)

Yield strength and plasticity are responsible for the different wear behaviors between pristine Ti and BNNT-Ti MMCs. The representative tensile responses from Ti and BNNT-Ti composite are presented in Fig. 5. Compared to the yield strength (YS) of wrought Ti in tension, reported between 880 and 990 MPa in the literature [27], the spark plasma-sintered (SPS-ed) Ti in the present investigation exhibited yield stress of 921 ± 31 MPa. This attests to the high degree of densification of greater than 98%. For the same reason, compared to an ultimate tensile strength (UTS) of around 1008 MPa in wrought condition, SPS-ed Ti exhibited a UTS of 1029 ± 18 MPa. A significant strengthening was achieved in the BNNT-Ti composite due to the dispersion and integration of these high-strength reinforcements. The yield strength increased by 21.6% to 1120 ± 25 MPa, while the UTS increased by 10.7% to 1139 ± 18 MPa. However, this strengthening does come at the expense of the amount of strain the composite can sustain. The strain till necking in BNNT-Ti was reduced to 0.1, a 37.5% reduction than 16 in Ti (Fig. 5). The greater ductility explained the severe plastic deformation in pristine Ti samples during wear.

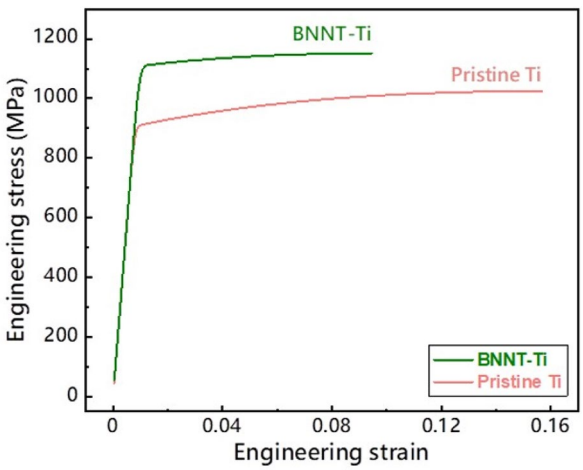

Figure 5: Representative bulk tensile plasticity of Ti and Ti-BNNT measured by PIP technique. The yield strength of the BNNT-Ti composite improved by 21.6% to 1120 MPa, while the UTS was enhanced by 10.7% to 1139 MPa. On the other hand, the ductility till necking was reduced by 37.5% to 0.1 in the BNNT-Ti composite.

Radiation shielding properties of BNNT-Ti MMCs

Our previous work showed that the reduction of SPS temperature played a substantial role in the retention and survival of BNNTs in the Ti matrix. Bustillos et al. have observed remarkable survival of BNNTs at a sintering temperature of 750 °C [18]. Since BNNT is the effective component for radiation shielding, a lower sintering temperature, 750 °C, was selected to preserve BNNTs during sintering [23–25]. At a higher sintering temperature, 950 °C, many BNNTs reacted with the Ti matrix and formed TiB whiskers. The improved survival of BNNTs does come at the cost of a reduction in densification, which could deteriorate the mechanical performances of BNNT-Ti composites. Hence, the sintering temperature of 750 °C was not adapted for the mechanical and tribological evaluations. Table 2 summarizes the geometric information on both pristine Ti and BNNT-Ti samples.

The neutron radiation results can also be found in Table 2. Both linear and mass absorption coefficients are calculated to elucidate the effect of BNNTs on neutron radiation shielding. The results were further normalized against pristine Ti (750 °C) to highlight the changes in all samples (Fig. 6). Both pristine Ti samples showed the same radiation shielding effectiveness. The only difference between the two pristine Ti samples is the overall densification. Ti with lower sintering temperatures has higher porosity. The increased porosity did not play any significant role in radiation shielding. The highest neutron attenuation was measured in the case of BNNT-Ti (750 °C), where 45 and 50% improvement in linear and mass absorption coefficients were obtained with only 1 wt% of BNNT. When sintered at 950 °C, the BNNT-Ti sample with the same amount of BNNTs showed only a 10% improvement in the neutron radiation shielding performance. As the sintering temperature of the SPS process increased, the interfacial reactions became progressively aggressive, resulting in the loss of the BNNT phase and thus lower radiation attenuation. Due to the possible residual oxide present in the metal and BNNT, boron elements in the BNNT phase, including amorphous boron impurities, can be oxidized, forming boron oxides. Boron trioxide, B_2O_3, is a stable form of boron oxide with a melting point of 450 °C and boiling point

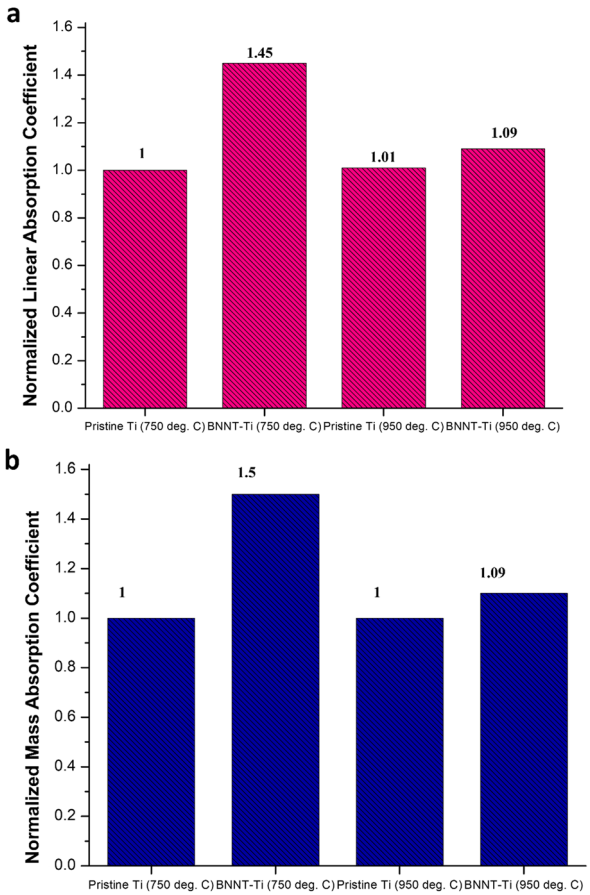

Figure 6: Normalized neutron radiation shielding results for Ti and BNNT-Ti composites sintered at 750 °C and 950 °C. (a) Normalized linear absorption coefficients, (b) normalized mass absorption coefficients.

of 1860 °C. However, the possible formation of volatile boron suboxide such as B_2O_2 can be attributed to the loss of boron which is highly effective in neutron absorption.

Figure 7 exhibits the fracture surface of BNNT-Ti sintered at 750 °C. BNNTs are found in the 750 °C samples retained with the original tubular morphologies. BNNTs tend to lodge at the grain boundaries. The tubular BNNTs (Fig. 7a) indicate a lesser interfacial reaction between the BNNTs and titanium matrix than the sample sintered at 950 °C. (Fig. 7b). These results suggest that the retention of BNNTs is crucial to the radiation shielding performance of the metal matrix composites. A trade-off between the mechanical properties and the radiation shielding performance must be considered.

Conclusions

The present work evaluated the tribological and radiation shielding behavior of pristine Ti and BNNT-Ti MMCs. Zircon simulant was used in the current work to represent the most abrasive condition on the lunar surface. The addition of BNNTs improved the wear resistance of titanium. BNNT-Ti MMCs showed 10.2 and 25.5% improvements in wear volume loss compared to pristine Ti samples with and without lunar simulants, respectively. The increased hardness and yield strength are the main reasons for the improved wear behavior. PIP testing was conducted on pristine Ti and BNNT-Ti MMCs to evaluate the effects of BNNTs addition on the tensile plasticity of Ti. The yield and ultimate tensile strength increased by 21.6% and 10.7%, respectively. However, the ductility has been reduced by 37.5% compared to the unreinforced Ti. BNNT-Ti samples also showed excellent neutron attenuation properties. The linear absorption coefficient has increased by 45%. A 50% improvement was observed in the mass absorption coefficient in the BNNT-Ti sample. The maximum radiation shielding performance was found in the BNNT-Ti MMC sintered at a lower temperature (750 °C), where the BNNTs were mostly retained

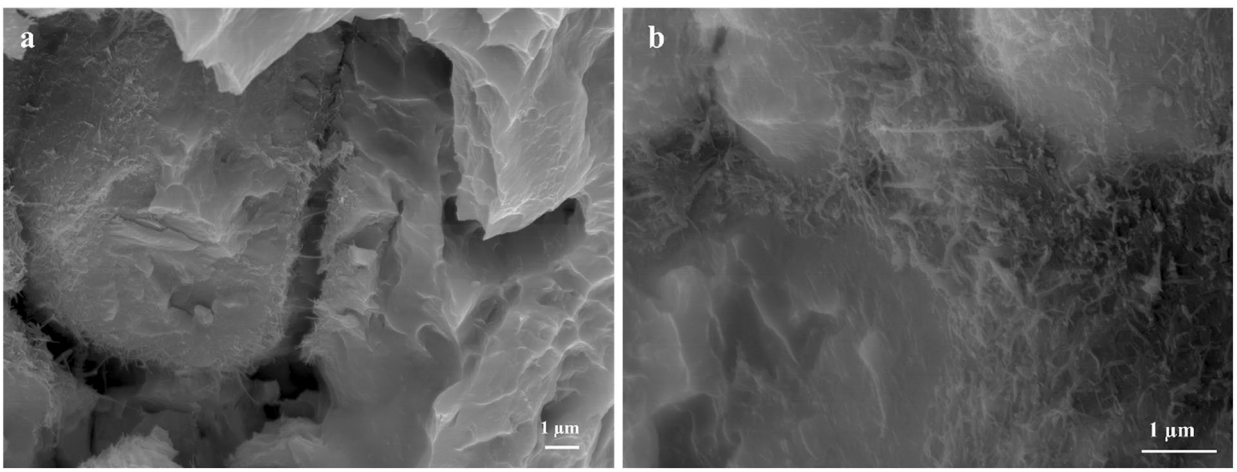

Figure 7: Fracture surface of (a) BNNT-Ti sintered at 750 °C showing retained BNNTs between the grains (fibrous feature) and (b) on the surface of Ti grains.

during sintering. However, the overall densification dropped from 98.4 to 95.5%. The reduction in densification may lead to deterioration in mechanical properties. Hence, a tradeoff between mechanical and radiation shielding properties should always be considered for future BNNT-Ti composite designs.

Materials and experimental details

Powder preparation

Pristine Ti6Al4V powders and mixed BNNT-Ti (BNNT-Ti64) powders are seen in Fig. 8. The initial BNNTs are received in the form of puffballs with lengths between 100 and 200 μm. Figure 8(a and b) shows the highly entangled puffballs and an SEM micrograph of the BNNT puffball. Overall uniform dispersion of BNNTs has been achieved after ultrasonication treatment in acetone for 45 min, followed by titanium powder addition and magnetic stirring. The detailed procedure for powder preparation can be found in our previous work [18]. A certain degree of agglomeration can also be seen in the mixed particles, as shown in Fig. 8d. The densification of the samples was performed using a Thermal Technologies model 10-4 spark plasma sintering (SPS) apparatus (Thermal Technologies, LLC, Santa Rosa, CA) with a standard 20 mm diameter graphite die. The powders were sintered under vacuum with sintering parameters of a maximum temperature of 950 °C and a maximum pressure of 60 MPa. The dwell time is set to be 10 min. A custom-made die with a 26 mm diameter was used to prepare samples for radiation shielding testing. An additional set of samples was sintered at 750 °C with sintering pressure at 60 MPa to prevent BNNTs reaction with Ti matrix [18].

Tribological testing

Wear experiments were conducted using the ball-on-disk tribometer (NANOVEA, Irvine, CA) with a 3-mm Aluminum Oxide ball (Ra = 15.4 nm) to determine titanium's change in wear resistance with BNNT addition. A load of 5 N was applied for 30 min at a speed of 50 RPM over a wear track diameter of 3 mm. The coefficient of friction was recorded during the wear test. For characterization of wear volume, a non-contact

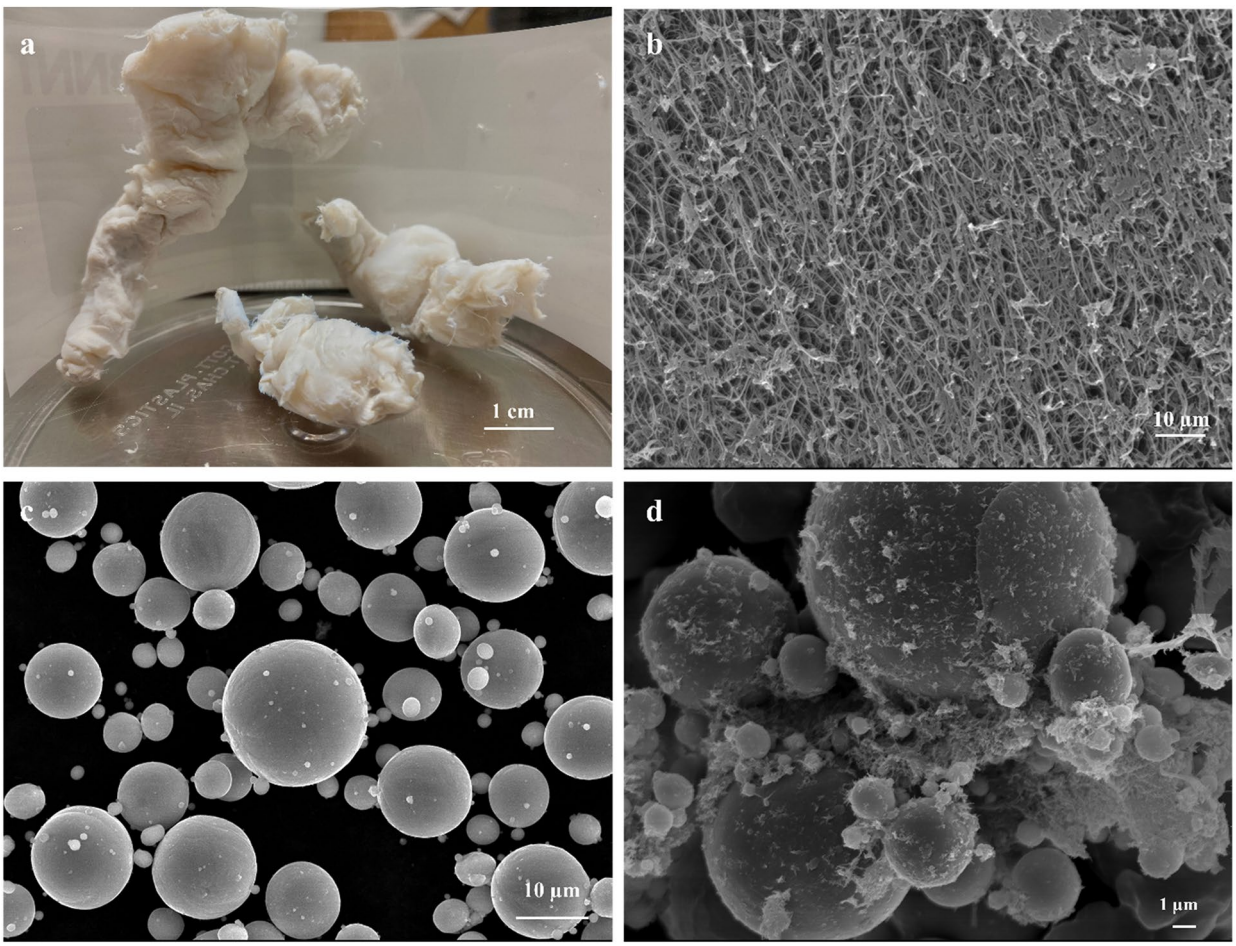

Figure 8: SEM images of (a) as received BNNT puffballs, (b) high magnification image of BNNTs, (c) Ti6Al4V powder, and (d) mixed BNNT-Ti powders. Severely clustered BNNT puffballs are reasonably well dispersed on Ti6Al4V powders.

profilometer (NANOVEA, Irvine, CA) was used to scan the wear track. The wear volume was calculated by doing a cross-sectional area analysis of the wear track using the Scanning Probe Image Processor (SPIP) software (Hørsholm, Denmark) and multiplying the area by the circumference of the wear track. A scanning electron microscope (SEM) (JEOL, F100) (Peabody, MA) was also used to image the wear tracks. To compare the performance of the BNNT-Ti samples against wear by lunar regolith particles, a methodology for testing three-body wear with lunar regolith simulants was implemented by designing a fixture to hold the simulant inside the wear track. The fixture, shown in Fig. S1 (supplementary information), was attached to the tribometer stage, and the sample was secured inside. The simulant was poured inside the fixture, ensuring the sample's surface was entirely covered by the simulant before the test began.

From the soil samples from the Apollo missions, the regolith composition has been identified to have a more uniform composition than terrestrial soil [6]. The regolith can vary in composition and particle size throughout different lunar regions. Hence, multiple Lunar regolith simulants have been created to simulate the different landing zones on the lunar surface. The zircon minerals, traced on the soil samples from all missions except Apollo 16, have been replicated with a simulant composed of terrestrial zircon minerals with similar properties. The zircon simulant is much more abrasive than another lunar regolith, as it is typically formed as part of the larger lunar breccias in the lowlands [28]. The zircon simulants mainly consist of ZrO_2 and SiO_2 with a trace amount of Fe_2O_3, assessed by X-ray diffraction. It has an average size of 88.5 ± 29.1 µm. The morphology of zircon can be seen in Fig. S2 (supplementary information).

Profilometry-based indentation plastometry (PIP)

The bulk tensile strength and plasticity of pristine Ti and BNNT-Ti composites were evaluated using the profilometry-based indentation plastometry (PIP) technique (Plastometrex, PLX Indentation Plastometer, v.1.0). Bulk tensile testing is the first choice to evaluate the samples' plasticity. However, performing bulk tensile testing is an increasing challenge in advanced functional materials due to the sample size limitation and availability. Profilometry-based Indentation Plastometry (PIP) is a novel, high-throughput technique that measures tensile stress–strain plasticity from a single indentation using a desktop indentation plastometer presented in Fig. S3a and b (supplementary information) [29, 30]. This is achieved in three steps in an integrated experimental-finite element modeling (FEM) operation. First, a spherical tungsten carbide-cobalt cermet indenter with a radius of 1 mm is used to indent the sample surface in displacement-controlled mode. A spherical indenter captures the plastic strain field as it varies with increasing penetration depth, thus reducing the possibility of similar force–displacement responses resulting solely from geometrically self-similar pyramidal or flat indenters [31]. It also generates a radially symmetric strain field in a spark plasma-sintered isotropic metal, thus achieving complete agreement between the experimental indentation response and the FEM simulation [32]. This step was used to record the force–displacement response from Ti and BNNT-Ti composite presented in Fig. S3c (supplementary information).

In the second step, a contacting stylus type Taylor-Hobson profilometer [33] equipped with a wide-range inductive gauge and a conical recess tip of radius 2 µm was used to acquire the two-dimensional (2D) surface profiles of the residual indent. Two axially symmetric surface scans were captured in mutually perpendicular horizontal directions, both through the central axis of the indent. Representative half-profiles of these axially symmetric scans acquired from Ti and BNNT-Ti are presented in Fig. S4 (supplementary information). It is observed that the depths of the residual indents are about 80 µm and their diameters are about 1000 µm. The grain size of pristine Ti and BNNT-Ti composite is about 10 µm. Thus, the diameters of the indents are representative of a more significant number of about 100 grains. Similarly, the depths of indents also represent about 8 grains. Thus, these large indents represent the plastic deformation in a large number of about 800 grains. It can be concluded that these force–displacement and stress–strain responses represent the macroscopic tensile plasticity characteristics of the bulk materials [34–36].

In the third step, the force–displacement response (Fig. S3c) and the residual depth profiles (Fig. S4) are integrated with an iterative finite element modeling (FEM) routine. A constitutive law describing the plastic work hardening behavior of the material, represented by the Voce equation [37, 38],

$$\sigma = \sigma_S - \left\{(\sigma_S - \sigma_Y) exp\left(\frac{-\varepsilon}{\varepsilon_o}\right)\right\}, \quad (1)$$

where σ (MPa) is the stress as a function of strain, ε, σ_S is the saturation stress, σ_Y is the yield stress, and ε_o is the characteristic strain for the exponential approach of stress to its saturation is solved to obtain the bulk tensile response and enumerate the plasticity parameters therein. The iterative FEM simulation was performed by a finite element modeling software (SEMPID, Software for the Extraction of Material Properties from Indentation Data). Three stress–strain responses were recorded to capture the statistical variation in the mechanical response of these composites, and the resultant average tensile properties were reported.

Radiation shielding testing

The radiation shielding testing was conducted at NASA Langley Research Center to test the neutron shielding capability

of the samples. The testing consisted of neutron exposure, radiation counting, and evaluation. For a neutron activation, a circular piece of pure indium (In) foil with a diameter of 25 mm and a thickness of around 1.0 mm was covered with each sample as a shielding material. The In foil was exposed to one-Curie americium (^{241}Am)-beryllium (^{9}Be) neutron source through the shielding material in the test, as shown in Fig. S5 (Supplementary Information). A polyethylene (PE) block of around 1 inch thickness was placed in front of the Am-Be neutron source to slow down the fast neutrons (4.5 MeV) from ^{241}Am-Be source (1 Ci). The PE block moderator decreased the dose rate of neutrons from 800 to 320 mrem/h. Indium foil and test material were taped to the PE block and exposed to the neutron irradiation at a dose rate of 320 mrem/h so that the ^{115}In could be activated to ^{116}In by neutrons. The neutron exposure was conducted overnight for the activation equilibrium. On the next day, the activated indium foil was removed from the test sample and counted using a Geiger–Mueller (GM) probe with a digital counter (SpecTech ST360, TN). The neutron shielding effectiveness was determined by the linear absorption cross-section (or coefficient, μ_x) and mass absorption cross-section (or coefficient, μ_m) of the material. Both coefficients can be calculated using Eqs. 2 and 3:

$$\mu_x = -\frac{1}{t}\ln\left(\frac{A}{A_0}\right), \tag{2}$$

$$\mu_m = \frac{\mu_x}{d} = -\frac{1}{d \bullet t}\ln\left(\frac{A}{A_0}\right), \tag{3}$$

where t is the sample thickness, d is the sample density, A_o is the average initial activity of unshielded In foil, and A is the average initial activity of shielded foil.

Acknowledgments

The authors acknowledge the financial support from NASA through grant 80NSSC20M0175 and the characterization facilities provided by Advanced Materials Engineering Research Institute (AMERI) at FIU.

Funding

Arvind Agarwal acknowledges the funding received from NASA through grant 80NSSC20M0175.

Data availability

Data will be available if requested.

Code availability

Not applicable.

Declarations

Conflict of interest The authors have no conflict of interest to declare.

Supplementary Information

The online version contains supplementary material available at https://doi.org/10.1557/s43578-022-00708-w.

References

1. C. Lutjering, J.C. William, *Titanium*, 2nd edn. (Springer, New York, 2007)
2. M.D. Hayat, H. Singh, Z. He, P. Cao, Titanium metal matrix composites: An overview. Compos. A Appl. Sci. Manuf. **121**, 418–438 (2019). https://doi.org/10.1016/j.compositesa.2019.04.005
3. C. Cui, B. Hu, L. Zhao, S. Liu, Titanium alloy production technology, market prospects, and industry development. Mater. Des. **32**(3), 1684–1691 (2011). https://doi.org/10.1016/j.matdes.2010.09.011
4. R.R. Boyer, An overview on the use of titanium in the aerospace industry. Mater. Sci. Eng. A **213**(1–2), 103–114 (1996). https://doi.org/10.1016/0921-5093(96)10233-1
5. D. Vaniman, R. Reedy, G. Heiken, G. Olhoeft, W. Mendell, The lunar environment. *The lunar Sourcebook*, CUP (1991), pp 27–60
6. J.E. Colwell, S. Batiste, M. Horányi, S. Robertson, S. Sture, Lunar surface: Dust dynamics and regolith mechanics. Rev. Geophys. **45**(2), 10 (2007). https://doi.org/10.1029/2005RG000184
7. Gaier, J.R., 2007. *The effects of lunar dust on EVA systems during the Apollo missions* (No. NASA/TM-2005-213610/REV1).
8. N.A. Schwadron, T. Baker, B. Blake, A.W. Case, J.F. Cooper, M. Golightly, A. Jordan, C. Joyce, J. Kasper, K. Kozarev, J. Mislinski, Lunar radiation environment and space weathering from the Cosmic Ray Telescope for the Effects of Radiation (CRaTER). J. Geophys. Res. **117**(E12), 10 (2012). https://doi.org/10.1029/2011JE003978
9. W.D. Carrier III, G.R. Olhoeft, W. Mendell, Physical properties of the lunar surface. *Lunar sourcebook* (1991), pp. 475–594
10. G. Chin, S. Brylow, M. Foote, J. Garvin, J. Kasper, J. Keller, M. Litvak, I. Mitrofanov, D. Paige, K. Raney, M. Robinson, Lunar Reconnaissance Orbiter overview: The instrument suite and mission. Space Sci. Rev. **129**(4), 391–419 (2007). https://doi.org/10.1007/s11214-007-9153-y
11. M.S. Clowdsley, J.W. Wilson, M.H.Y. Kim, R.C. Singleterry, R.K. Tripathi, J.H. Heinbockel, F.F. Badavi, J.L. Shinn, Neutron environments on the Martian surface. Phys. Med. **17**, 94–96 (2001)
12. J.W. Wilson, M.S. Clowdsley, J.L. Shinn, R.C. Singleterry, R.K. Tripathi, F.A. Cucinotta, J.H. Heinbockel, F.F. Badavi, W. Atwell, Neutrons in space: Shield models and design issues. No. 2000-01-2414. SAE Technical Paper, 2000. https://doi.org/10.4271/2000-01-2414

13. J. Köhler, C. Zeitlin, B. Ehresmann, R.F. Wimmer-Schweingruber, D.M. Hassler, G. Reitz, D.E. Brinza, G. Weigle, J. Appel, S. Böttcher, E. Böhm, Measurements of the neutron spectrum on the Martian surface with MSL/RAD. J. Geophys. Res. **119**(3), 594–603 (2014). https://doi.org/10.1002/2013JE004539
14. N.G. Chopra, R.J. Luyken, K. Cherrey, V.H. Crespi, M.L. Cohen, S.G. Louie, A. Zettl, Boron nitride nanotubes. Science **269**(5226), 966–967 (1995)
15. D. Golberg, Y. Bando, C.C. Tang, C.Y. Zhi, Boron nitride nanotubes. Adv. Mater. **19**(18), 2413–2432 (2007)
16. P. Nautiyal, C. Rudolf, A. Loganathan, C. Zhang, B. Boesl, A. Agarwal, Directionally aligned ultra-long boron nitride nanotube induced strengthening of aluminum-based sandwich composite. Adv. Eng. Mater. **18**(10), 1747–1754 (2016). https://doi.org/10.1002/adem.201600212
17. M.M.H. Bhuiyan, J. Wang, L.H. Li, P. Hodgson, A. Agarwal, M. Qian, Y. Chen, Boron nitride nanotube-reinforced titanium metal matrix composites with excellent high-temperature performance. J. Mater. Res. **32**(19), 3744–3752 (2017). https://doi.org/10.1557/jmr.2017.345
18. J. Bustillos, X. Lu, P. Nautiyal, C. Zhang, B. Boesl, A. Agarwal, Boron nitride nanotube-reinforced titanium composite with controlled interfacial reactions by spark plasma sintering. Adv. Eng. Mater. **22**(12), 2000702 (2020). https://doi.org/10.1002/adem.202000702
19. Q. Chao, S. Mateti, M. Annasamy, M. Imran, J. Joseph, Q. Cai, L.H. Li, P. Cizek, P.D. Hodgson, Y. Chen, D. Fabijanic, Nanoparticle-mediated ultra-grain refinement and reinforcement in additively manufactured titanium alloys. Addit. Manuf. (2021). https://doi.org/10.1016/j.addma.2021.102173
20. S.T. Abdulrahman, Z. Ahmad, S. Thomas, A.A. Rahman, *Introduction to neutron-shielding materials. In Micro and Nanostructured Composite Materials for Neutron Shielding Applications* (Woodhead Publishing, Sawston, 2020)
21. M. Ghazizadeh, J.E. Estevez, A.D. Kelkar, Boron nitride nanotubes for space radiation shielding. Int. J. Nano Stud. Technol **4**, 1–2 (2015). https://doi.org/10.19070/2167-8685-150007e
22. J.H. Kim, T.V. Pham, J.H. Hwang, C.S. Kim, M.J. Kim, Boron nitride nanotubes: Synthesis and applications. Nano Converg. **5**(1), 1–13 (2018). https://doi.org/10.1186/s40580-018-0149-y
23. J.H. Kang, G. Sauti, C. Park, V.I. Yamakov, K.E. Wise, S.E. Lowther, C.C. Fay, S.A. Thibeault, R.G. Bryant, Multifunctional electroactive nanocomposites based on piezoelectric boron nitride nanotubes. ACS Nano **9**(12), 11942–11950 (2015). https://doi.org/10.1021/acsnano.5b04526
24. S.A. Thibeault, J.H. Kang, G. Sauti, C. Park, C.C. Fay, G.C. King, Nanomaterials for radiation shielding. MRS Bull. **40**(10), 836–841 (2015). https://doi.org/10.1557/mrs.2015.225
25. S.H. Choi, R.W. Moses, C. Park, C.C. Fay, Multipurpose Cassegrain System, in *Earth and Space* (2020), pp. 1156–1165
26. D. Lahiri, V. Singh, A.K. Keshri, S. Seal, A. Agarwal, Carbon nanotube toughened hydroxyapatite by spark plasma sintering: Microstructural evolution and multiscale tribological properties. Carbon **48**(11), 3103–3120 (2010). https://doi.org/10.1016/j.carbon.2010.04.047
27. D. Banerjee, J.C. Williams, Perspectives on titanium science and technology. Acta Mater. **61**(3), 844–879 (2013). https://doi.org/10.1016/j.actamat.2012.10.043
28. C.A. Crow, S.A. Crowther, K.D. McKeegan, G. Turner, H. Busemann, J.D. Gilmour, Xenon systematics of individual lunar zircons, a new window on the history of the lunar surface. Geochim. Cosmochim. Acta **286**, 103–118 (2020). https://doi.org/10.1016/j.gca.2020.06.019
29. Y.T. Tang, J.E. Campbell, M. Burley, J. Dean, R.C. Reed, T.W. Clyne, Use of indentation plastometry to obtain stress-strain curves from small superalloy components made by additive manufacturing. SSRN (2020). https://doi.org/10.2139/ssrn.3708730
30. J. Dean, T.W. Clyne, Extraction of plasticity parameters from a single test using a spherical indenter and FEM modeling. Mech. Mater. **105**, 112–122 (2017). https://doi.org/10.1016/j.mechmat.2016.11.014
31. J.E. Campbell, R.P. Thompson, J. Dean, T.W. Clyne, Experimental and computational issues for automated extraction of plasticity parameters from spherical indentation. Mech. Mater. **124**, 118–131 (2018). https://doi.org/10.1016/j.mechmat.2018.06.004
32. J.E. Campbell, R.P. Thompson, J. Dean, T.W. Clyne, Comparison between stress-strain plots obtained from indentation plastometry, based on residual indent profiles, and from uniaxial testing. Acta Mater. **168**, 87–99 (2019). https://doi.org/10.1016/j.actamat.2019.02.006
33. Y.T. Tang, J.E. Campbell, M. Burley, J. Dean, R.C. Reed, T.W. Clyne, Profilometry-based indentation plastometry to obtain stress-strain curves from anisotropic superalloy components made by additive manufacturing. Materialia (2021). https://doi.org/10.1016/j.mtla.2021.101017
34. J.E. Campbell, H. Zhang, M. Burley, M. Gee, A.T. Fry, J. Dean, T.W. Clyne, A critical appraisal of the instrumented indentation technique and profilometry-based inverse finite element method indentation plastometry for obtaining stress-strain curves. Adv. Eng. Mater. **23**(5), 2001496 (2021). https://doi.org/10.1002/adem.202001496
35. T.W. Clyne, J.E. Campbell, M. Burley, J. Dean, Profilometry-based inverse finite element method indentation plastometry. Adv. Eng. Mater. **23**(9), 2100437 (2021). https://doi.org/10.1002/adem.202100437
36. M. Burley, J.E. Campbell, R. Reiff-Musgrove, J. Dean, T.W. Clyne, The effect of residual stresses on stress-strain curves obtained via profilometry-based inverse finite element method indentation plastometry. Adv. Eng. Mater. **23**(5), 2001478 (2021). https://doi.org/10.1002/adem.202001478

37. W. Gu, J. Campbell, Y. Tang, H. Safaie, R. Johnston, Y. Gu, C. Pleydell-Pearce, M. Burley, J. Dean, T.W. Clyne, Indentation plastometry of welds. Adv. Eng. Mater. (2022). https://doi.org/10.1002/adem.202101645
38. J.E. Campbell, M. Gaiser-Porter, W. Gu, S. Ooi, M. Burley, J. Dean, T.W. Clyne, Indentation plastometry of very hard metals. Adv. Eng. Mater. (2022). https://doi.org/10.1002/adem.202101398